Cu(II)-Doped $Cs_2SbAgCl_6$ Double Perovskite: A Lead-Free, Low-Bandgap Material

Abhoy Karmakar,[1] Mya S. Dodd,[1] Satyam Agnihotri,[1] Enrico Ravera,[2] and Vladimir K. Michaelis[1]*

1-Department of Chemistry, University of Alberta, Edmonton, Alberta, T6G 2G2, Canada

2-Magnetic Resonance Center (CERM), University of Florence and Consorzio Interuniversitario Risonanze Magnetiche di Metalloproteine, Via L. Sacconi 6, 50019 Sesto Fiorentino (FI), Italy and Department of Chemistry "Ugo Schiff", University of Florence, Via della Lastruccia 3, 50019 Sesto Fiorentino (FI), Italy

ABSTRACT

Lead-free halide double perovskites with a generic formula of $A_2B'(III)B''(I)X_6$ (A and B are cations and X is a halide anion) are being explored as a less toxic, higher thermal- and moisture-stable alternatives to well-studied lead halide perovskite ($APbX_3$) solar energy absorbers. However, the absorption profiles of most of the double perovskites reported to date have larger bandgaps (> 2 eV) that are poorly aligned with the solar spectrum, reducing their photoconversion efficiency. Here, we present new heterovalent paramagnetic Cu^{2+}-doped $Cs_2SbAgCl_6$ double perovskites that exhibit dramatic shifts in their bandgaps from ~ 2.6 eV ($Cs_2SbAgCl_6$, parent) to ~1 eV (Cu^{2+}-doped $Cs_2SbAgCl_6$). Powder X-ray diffraction patterns of the Cu^{2+}-doped polycrystalline materials indicate long-range crystallinity with non-uniform microstrain in the crystal lattice. To decode the dopant, complementary magnetic resonance spectroscopy techniques, solid-state nuclear magnetic resonance (NMR) and electron paramagnetic resonance (EPR), unravel the complex short- and medium-range structure of these novel double perovskite materials. Variable temperature ^{133}Cs NMR spectroscopy reveals that paramagnetic Cu^{2+} ions are incorporated within the double perovskite material impacting the ^{133}Cs NMR through a Fermi contact interaction. Finally, a comprehensive stress test of the material's long-term (up to 365 days) thermal and moisture stability indicate excellent resistance to environmental exposure.

INTRODUCTION

With an impressive increase in photoconversion efficiency (PCE) within the last decade,[1,2] hybrid organic–inorganic lead halide perovskites have prompted global research due to their potential use in high-efficiency solar cell technologies. However, despite their promising electronic properties and low production costs for photovoltaic and optoelectronic applications,[3–8] commercialization of lead halide perovskites has been hindered by their instability[9,10] as well as by long-term health and environmental concerns[11,12] mostly related to the leaching of Pb^{2+} due to their water-solubility.[13–15]

The general formula for perovskites of recent interest in photovoltaic research is ABX_3, where A = Cs^+, MA^+, or FA^+ (MA = methylammonium, FA = formamidinium), B = Pb^{2+} or Sn^{2+}, and X = Cl^-, Br^-, or I^-. An important property of these compounds is their bandgap tunability, achieved by modifications of the A, B and X positions. To improve the photovoltaic efficiency and stability of metal halide perovskites, alternative synthetic design approaches have included the incorporation of A-site mixed-cations,[6,16–18] mixed-halides,[19,20] as well as isovalent (Sn^{2+}, $Co^{2+,}$ Sr^{2+})[21–23] or heterovalent (Bi^{3+}, Au^{3+}, In^{3+})[24] B-site cations. These modifications influence the photovoltaic performance, optical properties, and, can lead to enhanced stability.[25–27] Although $MASnI_3$ is an attractive less toxic alternative to the isoelectronic Pb^{2+} sister materials, displaying a bandgap of 1.15 eV[28], it is unstable under ambient conditions due to rapid oxidation to Sn^{4+} which negatively impacts the photovoltaic properties of the material.[29]

Recent research has shown that replacing the B-site cation with a combination of trivalent (B'), and monovalent (B") cations results in the formation of $A_2B'B"X_6$, double perovskites that mimic the ABX_3 perovskite structure while displaying enhanced air and moisture stability,[30–35]

as well as bandgap tunability.[36–38] For example, Cs_2BiAgX_6 (X = Cl, Br) shows visible light absorption with indirect bandgaps of 2.77 and 1.95 eV for X = Cl and Br, respectively.[30,32] Similar bandgap tunability also has been observed by alloying of Sb^{3+} and In^{3+} in $Cs_2BiAgBr_6$.[36] In 2017, Deng *et al*.[39] successfully synthesized $Cs_2SbAgCl_6$ double perovskites with an indirect bandgap of 2.6 eV, while Tran *et al*.[37] prepared a series of B'-site mixed-cationic $Cs_2(Sb_xIn_{1-x})AgCl_6$ ($0 \leq x \leq 1$) double perovskites that show an indirect to direct bandgap modification. The structural and photophysical properties of nanocrystals,[40,41] low dimensional (i.e., 2D) double perovskites,[42] hysteresis-free solar cells,[43] and highly stable thin films[44] of $Cs_2BiAgBr_6$ double perovskite have recently been reported. A small bandgap Tl-containing $Cs_2AgTlBr_6$ double perovskite has emerged,[45] unfortunately, the acute toxicity of thallium makes it ill-suited to replace lead. A new class of layered double perovskite, namely, $Cs_4CuSb_2Cl_{12}$ displays a reduced bandgap, although at the cost of photovoltaic efficiency due to the restriction in structural dimensionality.[46,47] The search continues for a less-toxic, low-bandgap (ca. 1 – 1.4 eV) 3D double perovskite material synthesized from inexpensive and highly abundant elements.

Altering the optical and electronic properties for semiconductors is an attractive approach in modern device applications.[48,49] For example, homo- and heterovalent metal ion doped lead halide perovskites have been reported to enhance the optical and electronic properties of both nanocrystalline[50–53] and bulk materials[24,29,54] Likewise, double perovskites can be modified through a similar metal doping approach. For example, Slavney *et al.*[38] reduced the bandgap of $Cs_2BiAgBr_6$ by successful Tl-doping (a highly toxic metal), and Nandha and Nag[55] enhanced the visible light emission properties of $Cs_2InAgCl_6$ via Mn^{2+} doping. These observations inspired us to investigate the possibility of preparing de novo doped 3D double perovskite materials that yield reduced optical bandgaps for photovoltaic applications while maintaining desirable

practical properties. Herein, we describe the synthesis of a lead-free, inexpensive, and highly abundant element, heterovalent Cu^{2+} doping analogue of $Cs_2SbAgCl_6$ with a bandgap of ca. 1 eV.

The ns^2 outer shell electronic configuration of the B-site in 3D ABX_3 (B = Pb^{2+}, Sn^{2+}) perovskite structure is responsible for strong direct bandgap absorption and superior photovoltaic properties. Occupied and unoccupied $6s^2$ and $6p^0$ orbitals, respectively of Pb^{2+} contribute to form valence bond maxima (VBM) and conduction band minima (CBM), respectively.[56] $A_2B'B''X_6$ double perovskites allow a large diversity of B'- and B"-sites and hence diverse orbital compositions in its band edges. Since double perovskite materials exhibit dominant metal-to-metal charge transfer (MMCT) their electronic band structure relies heavily on the energies of B'- and B"-site metals' frontier orbitals.[45] For example, it has been shown when Pb^{2+} is replaced by isoelectronic Bi^{3+} and Tl^{+} in $MA_2BiTlBr_6$, a direct bandgap material is formed, whereas, replacing Tl^{+} with Ag^{+} yields an indirect bandgap material, $Cs_2BiAgBr_6$.[32,38] Similarly, the $Cs_2SbAgCl_6$ double perovskite shows an indirect bandgap transition, where the Sb-5s/Ag-4d and Sb-5p orbitals are the main contributors to the VBM and CBM, respectively.[37] Vargas et al. have reported a layered 2D double perovskite, $Cs_4Sb_2CuCl_{12}$, that exhibits a direct transition with a narrow bandgap (ca. 1 eV) due to the presence of an unpaired electron in Cu^{2+} ($3d^9$ configuration).[46] The $[CuCl_6]^{4-}$ octahedra are inserted between $[SbCl_6]^{3-}$ layers, corner sharing to each $[SbCl_6]^{3-}$ neighbor in the extended crystalline structure. These corner-shared octahedra are similar to the 3D perovskite network, which is crucial for their major photovoltaic success in lead-halide perovskites.[56] The much smaller bandgap of $Cs_4Sb_2CuCl_{12}$ is due to favorable orbital overlap of the Cu-3d orbitals with Cl- and Sb- orbitals, which broadens the VBM and minimizes the bandgap.[46] We hypothesized that dilute incorporation of $3d^9$ orbitals near to the VBM of

$Cs_2SbAgCl_6$ may allow us to narrow the bandgap while the 3D double perovskite structural network remains unaltered. Hence, we doped an impurity, Cu^{2+} into $Cs_2SbAgCl_6$ double perovskite. A closely related band edge modification has been reported by describing energy- and symmetry- matching of Tl-doped $Cs_2BiAgBr_6$ double perovskite.[38]

Solid-state nuclear magnetic resonance (NMR) spectroscopy is a powerful analytical tool that allows one to characterize atomic-level short- and medium-range structure, as well as dynamics in hybrid perovskites.[15,57–71] NMR spectroscopy was used to decode the local atomic structure of the $Cs_2SbAgCl_6$ parent and Cu^{2+}-doped $Cs_2SbAgCl_6$ double perovskite materials. In addition to NMR spectroscopy, powder X-ray diffraction (PXRD) was used to confirm the crystalline structure and phase purity, while optical properties were obtained using diffuse reflectance (DR). Materials were further characterized using field emission scanning electron microscopy (FESEM), energy dispersive X-ray (EDX), electron paramagnetic resonance (EPR) and thermogravimetric analysis (TGA) techniques. Finally, the long-term stability to environmental thermal and humidity stimuli of the materials was tested to assess their potential for long-term use as photovoltaic materials.

RESULTS AND DISCUSSION

The polycrystalline antimony-silver based double perovskite, $Cs_2SbAgCl_6$, was doped with Cu^{2+} by synthetic loading via solvent synthesis to produce $Cs_2Sb_{1-a}Ag_{1-b}Cu_{2x}Cl_6$ (a+b = 2x, x = 0.00 (i.e., parent compound), 0.01, 0.05, and 0.10). The nominal composition is reported due to the low Cu concentrations and associated challenges in elemental analysis of these materials (Table S1). Figure 1 shows photographs and the corresponding FESEM images for the $Cs_2SbAgCl_6$ parent and the Cu^{2+}-doped materials. The FESEM images confirm that the materials

are comprised of multi-faced micron-sized polycrystals. The PXRD pattern (Figures 2a & S1) of $Cs_2SbAgCl_6$, which match earlier reports,[39] indicate a face-centered cubic double perovskite structure ($Fm\bar{3}m$ space group) with $a = b = c = 10.699$ Å unit cell dimensions. The nearly identical PXRD patterns for $Cs_2SbAgCl_6$ and the doped materials indicate single-phase crystalline solids.

Closer examination of the PXRD patterns (Figure S2) indicates trace quantities of AgCl in the parent material, with increasing AgCl concentration as Cu is incorporated into the sample. Qualitatively, these findings may suggest that $[AgCl_6]^{5-}$ octahedra in the $Cs_2SbAgCl_6$ double perovskite lattice are being replaced by $[CuCl_6]^{4-}$ octahedra upon Cu^{2+} doping, forming vacancies to maintain charge balance and causing the formation of insoluble AgCl. The elemental analysis of these materials using EDX spectroscopy (Table S1) provides a clearer interpretation, indicating a decrease in Ag^+ concentration with increasing Cu^{2+} doping, while the concentrations of Cs^+, Sb^{3+}, and Cl^- are, within experimental uncertainty, unchanged. Note that the initial Sb^{3+}:Ag^+ loading ratios are kept constant at the beginning of the synthesis for all samples (see Supporting Information).

Scheme 1a displays the crystal structure of the $Cs_2SbAgCl_6$ double perovskite, showing that $[SbCl_6]^{3-}$ and $[AgCl_6]^{5-}$ octahedra are coordinated to each other in alternating corner-sharing configurations with a Cs^+ ion residing at the center of the cuboctahedra, thus maintaining an extended 3D perovskite crystal structure. There are in principle three positions in which Cu^{2+} can be incorporated into a double perovskite crystal lattice: the $[AgCl_6]^{5-}$ or the $[SbCl_6]^{3-}$ octahedra may be replaced by $[CuCl_6]^{4-}$ (Schemes 1b or 1c, respectively) or Cu^{2+} may occupy an A-site of the lattice (Scheme 1d), leading to the formation of a neighboring vacancy. Due to the large difference in the Pauling electronegativity (χ_P) of Cs (0.79) compared to that of Cu (1.90), a

structure that includes six covalent Cu-Cl bonds rather than 12 Cu-Cl ionic interactions is favored. Additionally, since χ_P for Ag (1.93) is very close to that for Cu but significantly different from that for Sb (2.05), the $[CuCl_6]^{4-}$ octahedra in the doped material are expected to primarily replace the $[AgCl_6]^{5-}$ octahedra, as illustrated in Scheme 1b. In summary, we hypothesize that substitution of Ag^+ by Cu^{2+} produces a Ag^+ cationic-vacancy to maintain charge balance neutrality of the doped materials. The EPR spectra (vide infra) of the sample at the lowest copper loading are consistent with the presence of tetragonally distorted $[CuCl_6]^{4-}$ octahedra:[72–74] the spectrum is substantially axial, with the downfield $g_{\|}$ feature, ~ 2.3, sizably broadened by unresolved hyperfine couplings, and with the $g_{\perp}$ component, ~ 2.0, shifted slightly upfield with respect to literature values. With increased doping, a peak at ~ 2.15 appears, indicating the presence of exchange-coupled copper pairs.[75] This intriguing observation suggests that copper-copper pairs form with a higher-than statistical probability. Exchange coupling is expected to emerge because of the interaction of the electrons on one copper center with electrons on another copper center, through the orbitals of intervening non-magnetic atoms between them.[75] This can happen through two bonds, as it would be for a Cu-Cl-Cu arrangement as well as through four bonds, as it would be for a Cu-Cl-M-Cl-Cu arrangement. A tempting explanation for the observed EPR spectrum is the formation of Cu-Cl-Cu pairs in the form of two elongated octahedra that share a vertex with orthogonal elongation axes. The emergence of such Cu-Cu pairs if the substitution was random would be expected around 6%, 30% and 60% for x = 0.01, 0.05 and 0.1 Cu^{2+} doped materials, respectively, including triplets and quartets.

The ionic radius for Cu^{2+} (0.87 Å) is slightly less than that for Sb^{3+} (0.90 Å) and significantly less than that for Ag^+ (1.29 Å);[76] thus, a decrease in the lattice parameter due to the

incorporation of Cu^{2+} into the crystal lattice is expected. For example, Figure 2b shows that the highly intense (220) peak in the PXRD pattern shifts slightly towards a higher 2θ value with copper incorporation, suggesting that the average lattice parameters are decreasing for the doped materials and that the Cu^{2+} ion has substituted into the lattice. The full width at half maximum (FWHM) of the diffraction peaks also increases systematically with increasing dopant concentration. These results imply local non-uniform microstrain structural defects in our doped materials (see below).[77] Such defects have also been observed in heterovalent Bi^{3+} doping of the $MAPbBr_3$ perovskite.[78] We have computed the extent of microstrain by measuring the FWHM values of the PXRD peaks in our materials with and without Cu^{2+} doping. The steadily increasing FWHM values (Figure 2c) are consistent with increased Cu^{2+} incorporation into the crystal lattice.

Similar to other halide double perovskites,[30,38] $Cs_2SbAgCl_6$ shows characteristics of a material with an indirect bandgap.[37,39] Figure 3a shows the DR and normalized absorbance spectrum of the $Cs_2SbAgCl_6$ parent and of the Cu^{2+}-doped (x = 0.10) double perovskites (see Figure S3 for the complete set of the series), which indicate a dramatic shift of the optical band edge upon Cu^{2+} doping. The Tauc plots (Figures 3b and 3c) show that Cu^{2+} doping (x = 0.10) reduces the indirect bandgap from 2.65 eV for $Cs_2SbAgCl_6$ to 1.02 eV. Assuming a direct allowed transition, Tauc plots give bandgaps of 2.84 eV for $Cs_2SbAgCl_6$ and 1.34 eV for the Cu^{2+} doped material (x = 0.10) (Figure S3). This finding is consistent with the pictures shown in Figure 1a, where a drastic visual color change from yellow to black occurs upon Cu^{2+} doping further supporting the reduction of the bandgap and hence absorb near-IR radiation. Similar observations have been reported in other doped double perovskite system[38], Cu^{2+} alloyed $Cs_4Sb_2MnCl_{12}$ material[79] and other Cu^{2+} containing perovskites[80]. We note that the band edge is

not sharp for the doped materials compared to that for $Cs_2SbAgCl_6$. This result suggests lattice disorder/defects in the doped materials and is consistent with the NMR results, discussed below. Band tailing is also observed in layered halide double perovskites,[42] thin film hybrid lead mixed-halide (Br, I) perovskite films,[81] and in doped lead halide perovskites.[24,78] Our experimental results agree well with past theoretical calculations by Volonakis et al.[82] who showed that the calculated indirect bandgaps are 2.6 and 2.1 eV for $Cs_2SbAgCl_6$ and $Cs_2SbCuCl_6$, respectively. Our experimental results show a similar decrease in the measured bandgap as copper is introduced into our materials. The stark difference between the experimental determined bandgap of our Cu^{2+} doped materials (vs. calculated $Cs_2SbCuCl_6$, diamagnetic, $3d^{10}$, Cu(I)) is attributed to the oxidation state; paramagnetic $3d^9$ Cu(II) enters the double perovskite lattice in the materials presented here.

It is worth mentioning that low doping concentrations of Cu^{2+} in $Cs_2SbAgCl_6$ double perovskite would cause a localized state near the band edges, which would be responsible for a localized transition. As the dopant Cu^{2+} concentration increases within the lattice, the average Cu-Cu distances between defect sites will decreases dramatically throughout the lattice. These localized impurity states will then form a delocalized state, resulting in an overall narrowing of the bandgap in higher doped materials. Similar effects have been reported in Tl-doped double perovskites and in other semiconducting doped systems.[38,83,84] Our experimental EPR results (above) show Cu^{2+} - Cu^{2+} coupling at higher Cu^{2+}-doping concentrations in $Cs_2SbAgCl_6$, supporting the possibility of forming a delocalized state due to suitable Cu-Cu distances.

The PXRD and DR results indicate local structural disorder within the doped double perovskites. To further elucidate these finer structural details, NMR spectroscopy, a powerful non-destructive analytical technique, was used to further decode the short- and medium-range

structure of the A (^{133}Cs) and B (^{121}Sb) sites. Figure 4a shows the ^{121}Sb NMR spectrum for nonspinning $Cs_2SbAgCl_6$ (x = 0.00) acquired at 21.1 T, displaying a sharp central transition resonance, centered at 817 ppm. Since $Cs_2SbAgCl_6$ has cubic symmetry and the Sb chemical environment has octahedral coordination to six Cl^- anions and the six next-nearest Ag^+ cations, second-order quadrupolar broadening is not expected.

Nevertheless, a broad underlying component spanning from ~1150 to 500 ppm is detected, which breaks into a series of spinning sidebands when spun at the magic-angle; this is attributed to signals from the satellite transitions for crystallites exhibiting slight imperfections/defects. Fitting data obtained using both nonspinning and magic-angle spinning data obtained at two magnetic field strengths (B_0 = 11.75 and 21.1 T) enables the determination of a small ^{121}Sb quadrupole coupling constant (C_Q) of 1.1 ± 0.3 MHz for the $Cs_2SbAgCl_6$ parent double perovskite (Figure S4a). This is consistent with other cubic antimony-containing complexes where even slight distortions about the symmetric Sb^{3+} nucleus can give rise to considerable quadrupole coupling constants with visible second-order broadening (e.g., C_Q = 2 to 3 MHz for K_2SbF_6), a consequence of the sizable ^{121}Sb quadrupole moment (–36.0 fm^2).[85]

Upon Cu^{2+} incorporation, a second broad ^{121}Sb NMR resonance appears to high frequency of the sharp resonance (Figure 4a). The breadth of the peak is attributed to the change in the electric field gradient about the $[SbCl_6]^{3-}$ octahedra that occur when neighboring Ag^+ cations are replaced by Cu^{2+}, i.e., $[(SbCl_6)Ag_5Cu]$, resulting in a sizeable quadrupole coupling (Figure S4b). Also, a systematic increase in the area of the peak centered at ~900 ppm is observed (Figure S5). Due to the differences in quadrupole coupling constants between the two sites, we refrain from fitting the two resonances quantitatively, although qualitatively the broad resonance increases with Cu^{2+} doping. Closer examination of the central transition assigned to $[(SbCl_6)Ag_6]$ indicates

that this NMR site is also impacted by Cu^{2+} incorporation, with the FWHM of the peak at δ_{iso} = 817 ppm increasing from 2.8 ± 0.3 kHz (x = 0.00) to 7.5 ± 0.5 kHz (x = 0.10) (Figure S5). The broadening is attributed to a reduction of the medium-range cubic symmetry about Sb^{3+} as Cu^{2+} is incorporated into the cubic lattice, impacting the electric field gradient about Sb, and to the presence of a paramagnetic species (Cu^{2+}, d^9-system), which reduces the spin-lattice relaxation times (T_1) of ^{133}Cs and increases the NMR linewidths under magic-angle spinning (T_2*) for ^{133}Cs and ^{121}Sb NMR (Table S2). The ^{121}Sb Gaussian-like lineshape of the $Cs_2SbAgCl_6$ parent double perovskite is commonly observed in hybrid perovskites and is attributed to indirect spin-spin coupling (*J*-coupling) between ^{121}Sb and the six coordinated $^{35/37}Cl$ anions (see Supporting Information).[85]

Figure 4b shows the ^{133}Cs MAS NMR spectra of $Cs_2SbAgCl_6$ with and without Cu^{2+}-doping. The small quadrupole moment for ^{133}Cs, $Q = -0.34$ fm^2, and high nuclear spin, $I = 7/2$, combined with its 100 % natural abundance, make it an attractive NMR nucleus that behaves as a pseudo $I = 1/2$ nuclear spin.[86] Since Cs^+ resides in a cubooctahedral void surrounded by alternating $[SbCl_6]^{3-}$ and $[AgCl_6]^{5-}$ octahedra (Scheme1a), it is an ideal method to probe local structural defects within the $Cs_2SbAgCl_6$ lattice as there is only one crystallographic position for this nucleus. A peak at δ_{iso} = 82 ppm in the ^{133}Cs MAS NMR spectra (labeled Peak-1 in Figure 4b) is observed for all samples. A new resonance emerges at δ_{iso} = –10 ppm (Peak-2), as Cu^{2+} is incorporated. Since we expect Cu^{2+} to substitute Ag^+, this peak is tentatively assigned to a Cs^+ surrounded by four Sb^{3+}, three Ag^+, and one Cu^{2+} (Scheme 1b and Figure S6b). As the Cu^{2+} doping increases further (x ≥ 0.05), a third resonance begins to emerge at δ_{iso} = −100 ppm (Peak-3) albeit with very low intensity (< 3% at x = 0.10, Table S3), which we tentatively assign to

^{133}Cs nuclei proximate to two Cu^{2+} sites (Figure S6c). Peak-1 also broadens as the Cu^{2+} doping increases (Figures S7 and S8 and Tables S4 and S5) due to the incorporation of paramagnetic Cu^{2+}, as discussed above for the ^{121}Sb NMR spectra. In fitting the $\delta_{iso}(^{133}Cs)$ peaks, we found that the area for Peak-1 decreases linearly, whereas those for Peak-2 and Peak-3 increase linearly with Cu^{2+} doping (Figure 4c, Table S3). The incorporation of Cu^{2+} results in the appearance of new ^{133}Cs resonances, which exhibit a linear relationship with synthetic Cu-loading (Figure S9). Using these tentatively assigned ^{133}Cs chemical shifts, and knowledge that each copper will impact eight cesium atoms, we can also obtain an estimate of Cu^{2+} incorporation post-synthesis (Table S1), although this does not account for potential Cu^{2+} clusters, and hence is expected to be a lower limit.

For the samples considered here, the first observation is that Peak-2 and Peak-3 are shifted to lower frequency. There are two mechanisms for paramagnetic shift: the through space interaction between the nuclear spin and the average magnetic moment of the paramagnetic center (pseudocontact shift) and the interaction between the nuclear spin and the unpaired spin density at the nucleus itself (Fermi contact).[87] Given that the pseudocontact contribution to the shift, based on the EPR spectrum (Figure 4d) and on geometrical arguments[87–90] is expected to be positive and smaller than 1 ppm (see Supporting Information), we conclude that the main source of the shift is Fermi contact. The fact that the shift is to lower frequency indicates that contact occurs through the spin-polarization mechanism.[91,92] The Fermi contact shift is the interaction of the nucleus with the unpaired spin electron density at the nucleus itself. Therefore, Fermi contact reports on the electronic structure about the nucleus. The observation of Fermi contact indicates that the nature of the interaction of the cesium ions with the lattice is not just ionic but has some

degree of covalency (i.e., orbital overlap). Finally, the mechanism of the Fermi contact suggests that the overlap is not with penetrating orbitals such as the 6s, but rather with p or d-type orbitals.

To further investigate the contributions from the paramagnetic Cu^{2+} center to the three distinct ^{133}Cs NMR chemical shifts discussed above, a series of variable-temperature ^{133}Cs NMR measurements from 238 to 343 K on the x = 0.10 Cu^{2+}-doped material was undertaken. The impact of paramagnetic species on the NMR spectra offers a wealth of information, encoded in the changes in chemical shifts and in a reduction of relaxation times as a consequence of the interaction between the nuclei and the unpaired electrons.[87,93] The observation of paramagnetic effects on the nuclei may provide substantial information about the electronic structure at the paramagnetic centers. The temperature dependence is a revealing feature of the behavior of paramagnetic systems and thus has proven useful in studies of a variety of solids.[91,94–104] All three ^{133}Cs NMR peaks shift to higher frequency as the temperature is increased (Figures 5a and 5b, and Table S6), but each has a distinct temperature dependence.[74-76,80,81] Peak-1 changes slowly with temperature; the small temperature dependence (0.08 ppm/K) for this peak is attributed to the temperature-induced changes in local structure, such as changes in the unit cell or position within the cuboctahedron (confirmed from variable temperature NMR spectroscopy on the $Cs_2SbAgCl_6$ parent material, Figure S10). In contrast, the much larger temperature dependence of the chemical shifts of Peak-2 and Peak-3 (0.35 ppm/K and 0.70 ppm/K, respectively) are a clear indication of the impact of neighboring Cu^{2+} ions, confirming that the Cs residing in the A site of the double perovskite is in proximity to the induced defect site with increasing incorporation of copper. Extrapolating to “infinite temperature” gives the diamagnetic isotropic chemical shift of ~ 96 ± 7 ppm, which is within the expected chemical shift range for the diamagnetic $Cs_2SbAgCl_6$ parent material (x = 0.00, $\delta_{iso}(^{133}Cs)$ = 85 ± 1 ppm) at 343 K (Figure

5c). The fact that the temperature dependence is Curie-like (i.e., the paramagnetic effect decreases with increasing temperature) and additive indicates that either contact occurs through two uncoupled copper centers or that the coupling between the two copper centers is smaller than the thermal energy (which is consistent with observations reported previously).[75,87]

Cesium-133 MAS NMR spectra, and PXRD patterns for cesium-containing chlorides, including CsCl, $Cs_3Sb_2Cl_9$, $Cs_4CuSb_2Cl_{12}$, and Cs_2CuCl_4, were acquired (Figure S11).[46,105] These spectra are distinct from those for $Cs_2SbAgCl_6$ parent and Cu^{2+}-doped materials. The distinct chemical shifts for each ^{133}Cs resonance as a function of temperature also correlate well with the EDX, ICP and PXRD results, vide supra, leading to further confidence that we are observing Cs^+ in a cuboctahedron with one and two Cu^{2+} neighbors; this is consistent with the structure expected for a Cu^{2+}-doped $Cs_2SbAgCl_6$ double perovskite and not from Cs-containing impurity phases.

LONGTERM STABILITY

A major concern with lead-containing hybrid perovskites is their low stability upon exposure to light, moisture and heat.[10,13–15] Therefore, we examined the moisture and thermal stability of both the $Cs_2SbAgCl_6$ parent and of the Cu^{2+}-doped materials. Polycrystalline materials were placed in a custom-built humidity chamber (Figure S12) with a relative humidity (RH) of 55 ± 5 % under otherwise normal laboratory conditions for 365 days (x = 0.00) and 30 days (x = 0.10). Based on analyses of the ^{133}Cs MAS NMR spectra (Figure 6a) and PXRD patterns (Figure 6b and 6b) and absorption spectra (Figure S13), there are no indications of decomposition from either material, and their bandgaps are retained under humid conditions. TGA indicates that materials with (x = 0.01) and without Cu^{2+} doping are stable up to 250 ^oC (Figure 6c), similar to

the thermal stability for the copper-antimony <111> perovskite (245 °C) reported by Vargas *et al.*[46] Long-term thermal stability studies were undertaken by heating these materials at 110 °C for six days under otherwise ambient conditions; ^{133}Cs NMR, PXRD and absorption spectra analysis (Figures 6a, 6b, and S13, respectively) again indicate high structural and optical stability with no evidence of decomposition.

CONCLUSIONS

In this work, we have investigated $Cs_2SbAgCl_6$ and its Cu^{2+}-doped double perovskite materials. The PXRD, EPR and NMR results indicate a well-ordered double perovskite cubic crystal structure with Cu^{2+} integrated into the lattice, creating local defect sites in multiple local Cs^+ and Sb^{3+} arrangements, whereby Cu^{2+} preferentially substitutes for Ag^+. These findings are further reinforced by EDX measurements and are consistent with Pauling electronegativity arguments. The optical properties of the material are directly related to the Cu^{2+} doping, which leads to a reduction of the optical indirect bandgap, from 2.65 eV for the parent material, to 1.02 eV for the x = 0.10 Cu^{2+}-doped material. The material's feasibility for photovoltaic applications was further examined through thermal and moisture exposure, demonstrating long-term structural and photophysical stability up to 365 days. Previously it has been shown that heterovalent doping in lead halide perovskites leads to an increase in conductivity and the formation of an n-type semiconductor.[54] Likewise, a series of DFT calculations for double perovskites including the parent compound studied here ($Cs_2SbAgCl_6$) indicate these materials exhibit small carrier effective masses (<0.4m_e), which are comparable to those calculated for $MAPbI_3$.[82,106] Although further study is needed, using these finding above, we propose that Cu^{2+}-doping creates a cation defect, which could lead to an increase in conductivity. In summary, the antimony-silver based double perovskites presented here exhibit several desirable properties in

comparison to lead halide perovskites including the potential for greater bandgap tunability, superior stability and comprised of inexpensive and highly abundant elements.

ASSOCIATED CONTENT

SUPPORTING INFORMATION

Detailed discussion of experimental techniques, powder XRD, EPR and NMR spectroscopy and optical bandgap measurement details are available in the Supporting Information.

AUTHOR INFORMATION

*Corresponding author: vladimir.michaelis@ualberta.ca

Note: The authors declare no competing financial interest.

ACKNOWLEDGEMENTS

The Natural Sciences and Engineering Research Council (NSERC) of Canada Discovery Grant and ATUMS training CREATE Programs, Canada Foundation for Innovation, Government of Alberta and Canada First Research Excellence Fund (Future Energy Systems, University of Alberta) are acknowledged for generous research support (VKM). MSD was partially supported by ECO-Canada through a SWILP internship. S.A. was partially supported by a UARE Scholarship of the University of Alberta. ER acknowledges support by Fondazione Cassa di Risparmio di Firenze, the University of Florence CERM-TT and the use of resources of Instruct-ERIC an ESFRI Landmark supported by national member subscriptions. Access to the 21.1 T NMR spectrometer was provided by the National Ultrahigh-Field NMR Facility for Solids (Ottawa, Canada), a national research facility funded by a consortium of Canadian Universities and by an NSERC RTI grant, supported by NSERC and Bruker BioSpin, and managed by the

University of Ottawa (www.nmr900.ca). The authors thank Dr. Victor Terskikh for assistance with NMR measurements at 21.1 T. The authors also thank members of the Michaelis group for many scientific discussions. AK dedicates this study to the late Tumpa Karmakar.

REFERENCES

(1) Kojima, A.; Teshima, K.; Shirai, Y.; Miyasaka, T. Organometal Halide Perovskites as Visible-Light Sensitizers for Photovoltaic Cells. *J. Am. Chem. Soc.* **2009**, *131*, 6050–6051.

(2) Green, M. A.; Hishikawa, Y.; Warta, W.; Dunlop, E. D.; Levi, D. H.; Hohl-Ebinger, J.; Ho-Baillie, A. W. H. Solar Cell Efficiency Tables (version 50). *Prog. Photovoltaics Res. Appl.* **2017**, *25*, 668–676.

(3) Tan, Z.-K.; Moghaddam, R. S.; Lai, M. L.; Docampo, P.; Higler, R.; Deschler, F.; Price, M.; Sadhanala, A.; Pazos, L. M.; Credgington, D.; et al. Bright Light-Emitting Diodes Based on Organometal Halide Perovskite. *Nat. Nanotechnol.* **2014**, *9*, 687–692.

(4) Zhu, H.; Fu, Y.; Meng, F.; Wu, X.; Gong, Z.; Ding, Q.; Gustafsson, M. V.; Trinh, M. T.; Jin, S.; Zhu, X. Y. Lead Halide Perovskite Nanowire Lasers with Low Lasing Thresholds and High Quality Factors. *Nat. Mater.* **2015**, *14*, 636–642.

(5) Xing, G.; Mathews, N.; Lim, S. S.; Yantara, N.; Liu, X.; Sabba, D.; Grätzel, M.; Mhaisalkar, S.; Sum, T. C. Low-Temperature Solution-Processed Wavelength-Tunable Perovskites for Lasing. *Nat. Mater.* **2014**, *13*, 476–480.

(6) Jeon, N. J.; Noh, J. H.; Yang, W. S.; Kim, Y. C.; Ryu, S.; Seo, J.; Seok, S. I. Compositional Engineering of Perovskite Materials for High-Performance Solar Cells. *Nature* **2015**, *517*, 476–480.

(7) Liu, M.; Johnston, M. B.; Snaith, H. J. Efficient Planar Heterojunction Perovskite Solar Cells by Vapour Deposition. *Nature* **2013**, *501*, 395–398.

(8) Shi, D.; Adinolfi, V.; Comin, R.; Yuan, M.; Alarousu, E.; Buin, A.; Chen, Y.; Hoogland, S.; Rothenberger, A.; Katsiev, K.; et al. Low Trap-State Density and Long Carrier Diffusion in Organolead Trihalide Perovskite Single Crystals. *Science* **2015**, *347*, 519–522.

(9) Yang, J.; Siempelkamp, B. D.; Mosconi, E.; De Angelis, F.; Kelly, T. L. Origin of the Thermal Instability in $CH_3NH_3PbI_3$ Thin Films Deposited on ZnO. *Chem. Mater.* **2015**, *27*, 4229–4236.

(10) Berhe, T. A.; Su, W.-N.; Chen, C.-H.; Pan, C.-J.; Cheng, J.-H.; Chen, H.-M.; Tsai, M.-C.; Chen, L.-Y.; Dubale, A. A.; Hwang, B.-J. Organometal Halide Perovskite Solar Cells: Degradation and Stability. *Energy Environ. Sci.* **2016**, *9*, 323–356.

(11) Needleman, H. Lead Poisoning. *Annu. Rev. Med.* **2004**, *55*, 209–222.

(12) Babayigit, A.; Ethirajan, A.; Muller, M.; Conings, B. Toxicity of Organometal Halide Perovskite Solar Cells. *Nat. Mater.* **2016**, *15*, 247–251.

(13) Herrera, P. A. M.; Kamat, P. V. Transformation of the Excited State and Photovoltaic Efficiency of $CH_3NH_3PbI_3$ Perovskite upon Controlled Exposure to Humidified Air. *J. Am. Chem. Soc.* **2015**, *137*, 1530−1538.

(14) Leguy, M. A.; Hu, Y.; Campoy-quiles, M.; Alonso, M. I.; Weber, O. J.; Azarhoosh, P.; Schilfgaarde, M. Van; Weller, M. T.; Bein, T.; Nelson, J.; et al. Reversible Hydration of $CH_3NH_3PbI_3$ in Films, Single Crystals, and Solar Cells. *Chem. Mater.* **2015**, *27*, 3397−3407.

(15) Askar, A. M.; Bernard, G. M.; Wiltshire, B.; Shankar, K.; Michaelis, V. K. Multinuclear Magnetic Resonance Tracking of Hydro, Thermal, and Hydrothermal Decomposition of $CH_3NH_3PbI_3$. *J. Phys. Chem. C* **2017**, *121*, 1013–1024.

(16) Saliba, M.; Matsui, T.; Seo, J. Y.; Domanski, K.; Correa-Baena, J. P.; Nazeeruddin, M. K.; Zakeeruddin, S. M.; Tress, W.; Abate, A.; Hagfeldt, A.; et al. Cesium-Containing Triple Cation Perovskite Solar Cells: Improved Stability, Reproducibility and High Efficiency. *Energy Environ. Sci.* **2016**, *9*, 1989–1997.

(17) Li, Z.; Yang, M.; Park, J. S.; Wei, S. H.; Berry, J. J.; Zhu, K. Stabilizing Perovskite Structures by Tuning Tolerance Factor: Formation of Formamidinium and Cesium Lead Iodide Solid-State Alloys. *Chem. Mater.* **2016**, *28*, 284–292.

(18) Zhang, M.; Yun, J. S.; Ma, Q.; Zheng, J.; Lau, C. F. J.; Deng, X.; Kim, J.; Kim, D.; Seidel, J.; Green, M. A.; et al. High-Efficiency Rubidium-Incorporated Perovskite Solar Cells by Gas Quenching. *ACS Energy Lett.* **2017**, *2*, 438–444.

(19) Eperon, G. E.; Leijtens, T.; Bush, K. A.; Green, T.; Wang, J. T.-W.; McMeekin, D. P.; Volonakis, G.; Milot, R. L.; Slotcavage, D. J.; Belisle, R.; et al. Perovskite-Perovskite Tandem Photovoltaics with Ideal Bandgaps. *Science* **2016**, *354*, 861−865.

(20) Tan, H.; Jain, A.; Voznyy, O.; Lan, X.; Arquer, F. P. G. de; Fan, J. Z.; Quintero-Bermudez, R.; Yuan, M.; Zhang, B.; Zhao, Y.; et al. Efficient and Stable Solution Processed Planar Perovskite Solar Cell via Contact Passivation. *Science* **2017**, *355*, 722–726.

(21) Lau, C. F. J.; Zhang, M.; Deng, X.; Zheng, J.; Bing, J.; Ma, Q.; Kim, J.; Hu, L.; Green, M. A.; Huang, S.; et al. Strontium-Doped Low-Temperature-Processed $CsPbI_2Br$ Perovskite Solar Cells. *ACS Energy Lett.* **2017**, *2*, 2319–2325.

(22) Zuo, F.; Williams, S. T.; Liang, P. W.; Chueh, C. C.; Liao, C. Y.; Jen, A. K. Y. Binary-Metal Perovskites Toward High-Performance Planar-Heterojunction Hybrid Solar Cells. *Adv. Mater.* **2014**, *26*, 6454–6460.

(23) Klug, M. T.; Osherov, A.; Haghighirad, A. A.; Stranks, S. D.; Brown, P. R.; Bai, S.; Wang, J. T. W.; Dang, X.; Bulović, V.; Snaith, H. J.; et al. Tailoring Metal Halide Perovskites through Metal Substitution: Influence on Photovoltaic and Material Properties. *Energy Environ. Sci.* **2017**, *10*, 236–246.

(24) Abdelhady, A. L.; Saidaminov, M. I.; Murali, B.; Adinolfi, V.; Voznyy, O.; Katsiev, K.; Alarousu, E.; Comin, R.; Dursun, I.; Sinatra, L.; et al. Heterovalent Dopant Incorporation for Bandgap and Type Engineering of Perovskite Crystals. *J. Phys. Chem. Lett.* **2016**, *7*, 295–301.

(25) Levchuk, I.; Osvet, A.; Tang, X.; Brandl, M.; Perea, J. D.; Hoegl, F.; Matt, G. J.; Hock, R.; Batentschuk, M.; Brabec, C. J. Brightly Luminescent and Color-Tunable Formamidinium Lead Halide Perovskite $FAPbX_3$ (X = Cl, Br, I) Colloidal Nanocrystals. *Nano Lett.* **2017**, *17*, 2765–2770.

(26) Hu, Y.; Bai, F.; Liu, X.; Ji, Q.; Miao, X.; Qiu, T.; Zhang, S. Bismuth Incorporation Stabilized α-$CsPbI_3$ for Fully Inorganic Perovskite Solar Cells. *ACS Energy Lett.* **2017**, *2*, 2219−2227.

(27) Lee, J.-W., Kim, D.-H., Kim, H.-S., Seo, S.-W., Cho, S.M., Park, N.-G. Formamidinium and Cesium Hybridization for Photo- and Moisture-Stable Perovskite Solar Cell. *Adv. Energy Mater.* **2015**, *5*, 1501310.

(28) Dang, Y.; Zhou, Y.; Liu, X.; Ju, D.; Xia, S.; Xia, H.; Tao, X. Formation of Hybrid Perovskite Tin Iodide Single Crystals by Top-Seeded Solution Growth. *Angew. Chem. Int. Ed.* **2016**, *55*, 3447–3450.

(29) Babu, R.; Giribabu, L.; Singh, S. P. Recent Advances in Halide-Based Perovskite Crystals and their Optoelectronic Applications. *Cryst. Growth Des.* **2018**, *18*, 2645–2664.

(30) Slavney, A. H.; Hu, T.; Lindenberg, A. M.; Karunadasa, H. I. A Bismuth-Halide Double Perovskite with Long Carrier Recombination Lifetime for Photovoltaic Applications. *J. Am. Chem. Soc.* **2016**, *138*, 2138−2141.

(31) Volonakis, G.; Haghighirad, A. A.; Milot, R. L.; Sio, W. H.; Filip, M. R.; Wenger, B.; Johnston, M. B.; Herz, L. M.; Snaith, H. J.; Giustino, F. $Cs_2InAgCl_6$: A New Lead-Free Halide Double Perovskite with Direct Band Gap. *J. Phys. Chem. Lett.* **2017**, *8*, 772–778.

(32) McClure, E. T.; Ball, M. R.; Windl, W.; Woodward, P. M. Cs_2AgBiX_6 (X = Br, Cl): New Visible Light Absorbing, Lead-Free Halide Perovskite Semiconductors. *Chem. Mater.* **2016**, *28*, 1348–1354.

(33) Filip, M. R.; Liu, X.; Miglio, A.; Hautier, G.; Giustino, F. Phase Diagrams and Stability of Lead-Free Halide Double Perovskites $Cs_2BB'X_6$: B = Sb and Bi, B′ = Cu, Ag, and Au, and X = Cl, Br, and I. *J. Phys. Chem. C* **2018**, *122*, 158–170.

(34) Jain, A.; Voznyy, O.; Sargent, E. H. High-Throughput Screening of Lead-Free Perovskite-like Materials for Optoelectronic Applications. *J. Phys. Chem. C* **2017**, *121*, 7183–7187.

(35) Wei, F.; Deng, Z.; Sun, S.; Zhang, F.; Evans, D. M.; Kieslich, G.; Tominaka, S.; Carpenter, M. A.; Zhang, J.; Bristowe, P. D.; et al. Synthesis and Properties of a Lead-Free Hybrid Double Perovskite: $(CH_3NH_3)_2AgBiBr_6$. *Chem. Mater.* **2017**, *29*, 1089–1094.

(36) Du, K. Z.; Meng, W.; Wang, X.; Yan, Y.; Mitzi, D. B. Bandgap Engineering of Lead-Free Double Perovskite $Cs_2AgBiBr_6$ through Trivalent Metal Alloying. *Angew. Chem. Int. Ed.* **2017**, *56*, 8158–8162.

(37) Tran, T. T.; Panella, J. R.; Chamorro, J. R.; Morey, J. R.; McQueen, T. M. Designing Indirect-Direct Bandgap Transitions in Double Perovskites. *Mater. Horizons* **2017**, *4*, 688–693.

(38) Slavney, A. H.; Leppert, L.; Bartesaghi, D.; Gold-Parker, A.; Toney, M. F.; Savenije, T. J.; Neaton, J. B.; Karunadasa, H. I. Defect-Induced Band-Edge Reconstruction of a Bismuth-Halide Double Perovskite for Visible-Light Absorption. *J. Am. Chem. Soc.* **2017**, *139*, 5015–5018.

(39) Deng, W.; Deng, Z.; He, J.; Wang, M.; Chen, Z.; Wei, S.; Feng, H.-J. Synthesis of $Cs_2AgSbCl_6$ and Improved Optoelectronic Properties of $Cs_2AgSbCl_6/TiO_2$ Heterostructure Driven by the Interface Effect for Lead-Free Double Perovskites Solar Cells. *Appl. Phys. Lett.* **2017**, *111*, 151602.

(40) Bekenstein, Y.; Dahl, J. C.; Huang, J.; Osowiecki, W. T.; Swabeck, J. K.; Chan, E. M.; Yang, P.; Alivisatos, A. P. The Making and Breaking of Lead-Free Double Perovskite Nanocrystals of Cesium Silver-Bismuth Halide Compositions. *Nano Lett.* **2018**, *18*, 3502-3508.

(41) Creutz, S. E.; Crites, E. N.; De Siena, M. C.; Gamelin, D. R. Colloidal Nanocrystals of Lead-Free Double-Perovskite (Elpasolite) Semiconductors: Synthesis and Anion Exchange to Access New Materials. *Nano Lett.* **2018**, *18*, 1118–1123.

(42) Connor, B. A.; Leppert, L.; Smith, M. D.; Neaton, J. B.; Karunadasa, H. I. Layered Halide Double Perovskites: Dimensional Reduction of $Cs_2AgBiBr_6$. *J. Am. Chem. Soc.* **2018**, *140*, 5235–5240.

(43) Pantaler, M.; Cho, K. T.; Queloz, V.; Garcia Benito, I.; Fettkenhauer, C.; Anusca, I.; Nazeeruddin, M. K.; Lupascu, D. C.; Grancini, G. Hysteresis-Free Lead-Free Double Perovskite Solar Cells by Interface Engineering. *ACS Energy Lett.* **2018**, *3*, 1781−1786.

(44) Greul, E.; Petrus, M. L.; Binek, A.; Docampo, P.; Bein, T. Highly Stable, Phase Pure $Cs_2AgBiBr_6$ Double Perovskite Thin Films for Optoelectronic Applications. *J. Mater. Chem. A* **2017**, *5*, 19972–19981.

(45) Slavney, A. H.; Leppert, L.; Saldivar Valdes, A.; Bartesaghi, D.; Savenije, T. J.; Neaton, J. B.; Karunadasa, H. Small-Bandgap Halide Double Perovskites. *Angew. Chem. Int. Ed.* **2018**, *57*, 12765 –12770.

(46) Vargas, B.; Ramos, E.; Pérez-Gutiérrez, E.; Alonso, J. C.; Solis-Ibarra, D. A Direct Bandgap Copper-Antimony Halide Perovskite. *J. Am. Chem. Soc.* **2017**, *139*, 9116–9119.

(47) Singhal, N.; Chakraborty, R.; Ghosh, P.; Nag, A. Low-Bandgap $Cs_4CuSb_2Cl_{12}$ Layered Double Perovskite: Synthesis, Reversible Thermal Changes, and Magnetic Interaction. *Chem. Asian J.* **2018**, *13*, 2085 –2092.

(48) Abram, R. A.; Rees, G. J.; Wilson, B. L. H. Heavily Doped Semiconductors and Devices. *Adv. Phys.* **1978**, *27*, 799–892.

(49) Piao, Y.; Meany, B.; Powell, L. R.; Valley, N.; Kwon, H.; Schatz, G. C.; Wang, Y. Brightening of Carbon Nanotube Photoluminescence through the Incorporation of sp^3 Defects. *Nat. Chem.* **2013**, *5*, 840–845.

(50) Misra, R. K.; Aharon, S.; Li, B.; Mogilyansky, D.; Visoly-Fisher, I.; Etgar, L.; Katz, E. A.

Temperature- and Component-Dependent Degradation of Perovskite Photovoltaic Materials under Concentrated Sunlight. *J. Phys. Chem. Lett.* **2015**, *6*, 326–330.

(51) Shao, H.; Bai, X.; Cui, H.; Pan, G.; Jing, P.; Qu, S.; Zhu, J.; Zhai, Y.; Dong, B.; Song, H. White Light Emission in Bi^{3+}/Mn^{2+} Ion Co-Doped $CsPbCl_3$ Perovskite Nanocrystals. *Nanoscale* **2018**, *10*, 1023–1029.

(52) Das Adhikari, S.; Dutta, A.; Dutta, S. K.; Pradhan, N. Layered Perovskites $L_2(Pb_{1-x}Mn_x)Cl_4$ to Mn-Doped $CsPbCl_3$ Perovskite Platelets. *ACS Energy Lett.* **2018**, *3*, 1247–1253.

(53) Meinardi, F.; Akkerman, Q. A.; Bruni, F.; Park, S.; Mauri, M.; Dang, Z.; Manna, L.; Brovelli, S. Doped Halide Perovskite Nanocrystals for Reabsorption-Free Luminescent Solar Concentrators. *ACS Energy Lett.* **2017**, *2*, 2368–2377.

(54) Zhou, Y.; Chen, J.; Bakr, O. M.; Sun, H. Metal-Doped Lead Halide Perovskites: Synthesis, Properties, and Optoelectronic Applications. *Chem. Mater.* **2018**, *30*, 6589−6613.

(55) K., N. N.; Nag, A. Synthesis and Luminescence of Mn-Doped $Cs_2AgInCl_6$ Double Perovskites. *Chem. Commun.* **2018**, *54*, 5205--5208.

(56) Yin, W.; Shi, T.; Yan, Y. Superior Photovoltaic Properties of Lead Halide Perovskites: Insights from First-Principles Theory. *J. Phys. Chem. C* **2015**, *119*, 5253−5264.

(57) Knop, O.; Wasylishen, R. E.; White, M. A.; Cameron, T. S.; Van Oort, M. J. M. Alkylammonium Lead Halides. Part 2. $CH_3NH_3PbX_3$ (X=Cl, Br, I) Perovskites: Cuboctahedral Halide Cages with Isotropic Cation Reorientation. *Can. J. Chem.* **1990**, *68*, 412–422.

(58) Kubicki, D. J.; Prochowicz, D.; Hofstetter, A.; Zakeeruddin, S. M.; Grätzel, M.; Emsley, L. Phase Segregation in Potassium-Doped Lead Halide Perovskites from ^{39}K Solid-State NMR at 21.1 T. *J. Am. Chem. Soc.* **2018**, *140*, 7232−7238.

(59) Senocrate, A.; Moudrakovski, I.; Kim, G. Y.; Yang, T.; Gregori, G.; Grätzel, M.; Maier, J. The Nature of Ion Conduction in Methylammonium Lead Iodide: A Multimethod Approach. *Angew. Chem. Int. Ed.* **2017**, *56*, 7755–7759.

(60) Fabini, D. H.; Siaw, T. A.; Stoumpos, C. C.; Laurita, G.; Olds, D.; Page, K.; Hu, J. G.; Kanatzidis, M. G.; Han, S.; Seshadri, R. Universal Dynamics of Molecular Reorientation in Hybrid Lead Iodide Perovskites. *J. Am. Chem. Soc.* **2017**, *139*, 16875–16884.

(61) Rosales, B. A.; Men, L.; Cady, S. D.; Hanrahan, M. P.; Rossini, A. J.; Vela, J. Persistent Dopants and Phase Segregation in Organolead Mixed-Halide Perovskites. *Chem. Mater.* **2016**, *28*, 6848–6859.

(62) Franssen, W. M. J.; Van Es, S. G. D.; Dervişolu, R.; De Wijs, G. A.; Kentgens, A. P. M. Symmetry, Dynamics, and Defects in Methylammonium Lead Halide Perovskites. *J. Phys. Chem. Lett.* **2017**, *8*, 61–66.

(63) Prochowicz, D.; Yadav, P.; Saliba, M.; Kubicki, D. J.; Tavakoli, M. M.; Zakeeruddin, S. M.; Lewiński, J.; Emsley, L.; Grätzel, M. One-Step Mechanochemical Incorporation of an Insoluble Cesium Additive for High Performance Planar Heterojunction Solar Cells. *Nano Energy* **2018**, *49*, 523–528.

(64) Wasylishen, R. E.; Knop, O.; Macdonald, J. B. Cation Rotation in Methylammonium Lead Halides. *Solid State Commun.* **1985**, *56*, 581–582.

(65) Karmakar, A.; Askar, A. M.; Bernard, G. M.; Terskikh, V. V.; Ha, M.; Patel, S.; Shankar, K.; Michaelis, V. K. Mechanochemical Synthesis of Methylammonium Lead Mixed-Halide Perovskites: Unraveling the Solid-Solution Behavior Using Solid-State NMR. *Chem. Mater.* **2018**, *30*, 2309–2321.

(66) Askar, A. M.; Karmakar, A.; Bernard, G. M.; Ha, M.; Terskikh, V. V.; Wiltshire, B. D.; Patel, S.; Fleet, J.; Shankar, K.; Michaelis, V. K. Composition-Tunable Formamidinium Lead Mixed Halide Perovskites via Solvent-Free Mechanochemical Synthesis: Decoding the Pb Environments Using Solid-State NMR Spectroscopy. *J. Phys. Chem. Lett.* **2018**, *9*, 2671–2677.

(67) Bernard, G. M.; Goyal, A.; Miskolzie, M.; McKay, R.; Wu, Q.; Wasylishen, R. E.; Michaelis, V. K. Methylammonium Lead Chloride: A Sensitive Sample for an Accurate NMR Thermometer. *J. Magn. Reson.* **2017**, *283*, 14–21.

(68) Bernard, G. M.; Wasylishen, R. E.; Ratcliffe, C. I.; Terskikh, V.; Wu, Q.; Buriak, J. M.; Hauger, T. Methylammonium Cation Dynamics in Methylammonium Lead Halide Perovskites: A Solid-State NMR Perspective. *J. Phys. Chem. A* **2018**, *122*, 1560–1573.

(69) Kubicki, D. J.; Prochowicz, D.; Hofstetter, A.; Saski, M.; Yadav, P.; Bi, D.; Pellet, N.; Lewiński, J.; Zakeeruddin, S. M.; Grätzel, M.; et al. Formation of Stable Mixed Guanidinium-Methylammonium Phases with Exceptionally Long Carrier Lifetimes for High-Efficiency Lead Iodide-Based Perovskite Photovoltaics. *J. Am. Chem. Soc.* **2018**, *140*, 3345–3351.

(70) Kubicki, D. J.; Prochowicz, D.; Hofstetter, A.; Zakeeruddin, S. M.; Grätzel, M.; Emsley, L. Phase Segregation in Cs-, Rb- and K-Doped Mixed-Cation $(MA)_x(FA)_{1-x}PbI_3$ Hybrid Perovskites from Solid-State NMR. *J. Am. Chem. Soc.* **2017**, *139*, 14173–14180.

(71) Kubicki, D. J.; Prochowicz, D.; Hofstetter, A.; Péchy, P.; Zakeeruddin, S. M.; Grätzel, M.; Emsley, L. Cation Dynamics in Mixed-Cation $(MA)_x(FA)_{1-X}PbI_3$ Hybrid Perovskites from Solid-State NMR. *J. Am. Chem. Soc.* **2017**, *139*, 10055–10061.

(72) Yang, M.; Wen-chen, Z.; Lv, H. Defect Structure and Spin-Hamiltonian Parameters for the $CuCl_6^{4-}$ Cluster in the Tetragonal $RbCdCl_3:Cu^{2+}$ crystal. *Spectrochim. Acta Part A Mol. Biomol. Spectrosc.* **2009**, *72*, 515–517.

(73) Wei, M.; Willett, R. D.; Hipps, K. W. EPR, Electronic, and Vibrational Spectra of the $CuCl_6^{4-}$ Anion in [tris(2-aminoethyl)amineH_4]$_2$ [$CuCl_6$]$Cl_4 \cdot 2H_2O$ and Crystal Structure of the Complex. *Inorg. Chem.* **1996**, *35*, 5300–5303.

(74) Mcdonald, R. G.; Hitchman, M. A. Electronic, EPR and Vibrational Spectra of the Hexachlorocuprate(4-) Ion. *Inorg. Chem.* **1989**, *28*, 3996–4001.

(75) Stratemeier, H.; Wagner, B.; Krausz, E. R.; Linder, R.; Schmidtke, H.; Pebler, J.; Hatfield, W. E.; ter Haar, L.; Reinen, D.; Hitchman, M. A. EPR and Electronic Spectra of (3-chloroanilinium)$_8$[$CuCl_6$]Cl_4: Evidence for Tetragonally Elongated $CuCl_6^{4-}$ Ions with the Long Axis Disordered in 2-Dimensions. *Inorg. Chem.* **1994**, *33*, 2320–2329.

(76) Shannon, B. Y. R. D.; H, M.; Baur, N. H.; Gibbs, O. H.; Eu, M.; Cu, V. Revised Effective Ionic Radii and Systematic Studies of Interatomie Distances in Halides and Chaleogenides. *Acta Cryst.* **1976**, *A32*, 751–767.

(77) Pramanick, A.; Wang, X. P.; Hoffmann, C.; Diallo, S. O.; Jørgensen, M. R. V; Wang, X. Microdomain Dynamics in Single-Crystal $BaTiO_3$ during Paraelectric-Ferroelectric Phase Transition Measured with Time-of-Flight Neutron Scattering. *Phys. Rev. B* **2015**, *92*, 174103.

(78) Nayak, P.; Sendner, M.; Wenger, B.; Wang, Z.; Sharma, K.; Ramadan, A. J.; Lovrincic, R.; Pucci, A.; Madhu, P. K.; Snaith, H. J. The Impact of Bi^{3+} Heterovalent Doping in Organic-Inorganic Metal Halide Perovskite Crystals. *J. Am. Chem. Soc.* **2018**, *140*, 574–577.

(79) Vargas, B., Torres-Cadena, R., Rodriguez-Hernádez, J. Gembicky, M., Xie, H., Jiménez-Mier, J., Liu, Y.; Menéndez-Proupin, E.; Dunbar, K. R.; Lopez, N., et al. Optical, Electronic, and Magnetic Engineering of ⟨111⟩ Layered Halide Perovskites. *Chem. Mater.* **2018**, *30*, 5315-5321.

(80) Cortecchia, D.; Dewi, H. A.; Yin, J.; Bruno, A.; Chen, S.; Baikie, T.; Boix, P. P.; Grätzel, M.; Mhaisalkar, S.; Soci, C.; et al. Lead-Free $MA_2CuCl_xBr_{4-x}$ Hybrid Perovskites. *Inorg. Chem.* **2016**, *55*, 1044–1052.

(81) Fedeli, P.; Gazza, F.; Calestani, D.; Ferro, P.; Besagni, T.; Zappettini, A.; Calestani, G.; Marchi, E.; Ceroni, P.; Mosca, R. Influence of the Synthetic Procedures on the Structural and Optical Properties of Mixed-Halide (Br, I) Perovskite Films. *J. Phys. Chem. C* **2015**, *119*, 21304−21313.

(82) Volonakis, G.; Filip, M. R.; Haghighirad, A. A.; Sakai, N.; Wenger, B.; Snaith, H. J.; Giustino, F. Lead-Free Halide Double Perovskites via Heterovalent Substitution of Noble Metals. *J. Phys. Chem. Lett.* **2016**, *7*, 1254–1259.

(83) Sunkara, S.; Vendra, V. K.; Jasinski, J. B.; Deutsch, T.; Andriotis, A. N.; Rajan, K.; Menon, M.; Sunkara, M. New Visible Light Absorbing Materials for Solar Fuels, $Ga(Sb_x)N_{1-x}$. *Adv. Mater.* **2014**, *26*, 2878–2882.

(84) Weyers, M.; Sato, M.; Ando, H. Red Shift of Photoluminescence and Absorption in Dilute GaAsN Alloy Layers. *Jpn. J. Appl. Phys.* **1992**, *31*, L853-L855.

(85) Faucher, A.; Terskikh, V. V; Wasylishen, R. E. Assessing Distortion of the AF_6(A=As, Sb) Octahedra in Solid Hexafluorometallates (V) via NMR Spectroscopy. *Can. J. Chem.*

2015, *93*, 938–944.

(86) Harris, R. K.; Becker, E. D.; de Menrzes, S. M. C.; Goodfellow, R.; Granger, P. Commission on Molecular Structure and Spectroscopy. *Pure Appl. Chem.* **2001**, *73*, 1795–1818.

(87) Bertini, I.; Luchinat, C.; Parigi, G.; Ravera, E. *NMR of Paramagnetic Molecules; Elsevier*; 2016.

(88) Van Vleck, J. H. The Theory of Electric and Magnetic Susceptibilities. *Oxford University Press*; 1932; p 226.

(89) Kurland, R. J.; Mcgarvey, B. R. Isotropic NMR Shifts in Transition Metal Complexes: The Calculation of the Fermi Contact and Pseudocontact Terms. *J. Magn. Reson.* **1970**, *2*, 286–301.

(90) Walder, B. J.; Patterson, A. M.; Baltisberger, J. H.; Grandinetti, P. J. Hydrogen Motional Disorder in Crystalline Iron Group Chloride Dihydrates. *J. Chem. Phys.* **2018**, *149*, 084503.

(91) Michaelis, V. K.; Greer, B. J.; Aharen, T.; Greedan, J. E.; Kroeker, S. Determining Electron Spin-Transfer Mechanisms in Paramagnetic Ba_2YMO_6 (M = Mo, Re, Ru) Double Perovskites by ^{89}Y and ^{137}Ba MAS NMR Spectroscopy. *J. Phys. Chem. C* **2012**, *116*, 23646−23652.

(92) Ceder, D.; Menetrier, M.; P, G. C.; Delmas, C.; Ceder, G. Understanding the NMR Shifts in Paramagnetic Transition Metal Oxides Using Density Functional Theory Calculations. *Phys. Rev. B* **2003**, *67*, 174103.

(93) La Mar, G. N.; Horrocks, W. E.; Holm, R. H. *NMR of Paramagnetic Molecules*; *Academic Press Inc.*, 1973.

(94) Wickramasinghe, N. P.; Ishii, Y. Sensitivity Enhancement, Assignment, and Distance Measurement in ^{13}C Solid-State NMR Spectroscopy for Paramagnetic Systems under Fast Magic Angle Spinning. *J. Magn. Reson.* **2006**, *181*, 233–243.

(95) Ooms, K.; Polenova, T.; Shough, A.; Doren, D. J.; Nash, M. J.; Lobo, R. F. Identification of Mixed Valence Vanadium in ETS-10 Using Electron Paramagnetic Resonance, ^{51}V Solid-State Nuclear Magnetic Resonance, and Density Functional Theory Studies. *J. Phys. Chem. C* **2009**, *113*, 10477–10484.

(96) Kermarrec, E.; Marjerrison, C. A.; Thompson, C. M.; Maharaj, D. D.; Levin, K.; Kroeker, S.; Granroth, G. E.; Flacau, R.; Yamani, Z.; Greedan, J. E.; et al. Frustrated FCC Antiferromagnet Ba_2YOsO_6: Structural Characterization, Magnetic Properties, and Neutron Scattering Studies. *Phys. Rev. B* **2015**, *075133*, 1–9.

(97) Grey, C. P.; Dupre, N. NMR Studies of Cathode Materials for Lithium-Ion Rechargeable Batteries. *Chem. Rev.* **2004**, *104*, 4493−4512.

(98) Ishii, Y.; Wickramasinghe, N. P.; Chimon, S. A New Approach in 1D and 2D ^{13}C High-

Resolution Solid-State NMR Spectroscopy of Paramagnetic Organometallic Complexes by Very Fast Magic-Angle Spinning. *J. Am. Chem. Soc.* **2003**, *125*, 3438–3439.

(99) Aguiar, P. M.; Katz, M. J.; Leznof, D. B.; Kroeker, S. Natural Abundance ^{13}C and ^{15}N Solid-state NMR Analysis of Paramagnetic Transition-metal Cyanide Coordination Polymers. *Phys. Chem. Chem. Phys.* **2009**, *11*, 6925–6934.

(100) Grey, C. P.; Smith, M. E.; Cheetham, A. K.; Dobson, C. M.; Dupree, R. MAS NMR Study of Rare-Earth Pyrochlores: Paramagnetic Shifts in the Solid State. *J. Am. Chem. Soc.* **1990**, *112*, 4670–4675.

(101) Brough, A. R.; Grey, C. P.; Dobson, C. M. Paramagnetic Ions as Structural Probes in Solid-State NMR: Distance Measurements in Crystalline Lanthanide Acetates. *J. Am. Chem. Soc.* **1993**, *115*, 7318–7327.

(102) Bertarello, A.; Schubeis, T.; Fuccio, C.; Ravera, E.; Fragai, M.; Parigi, G.; Emsley, L.; Pintacuda, G.; Luchinat, C. Paramagnetic Properties of a Crystalline Iron-Sulfur Protein by Magic-Angle Spinning NMR Spectroscopy. *Inorg. Chem.* **2017**, *56*, 6624–6629.

(103) Pell, A. J.; Middlemiss, D. S.; Strobridge, F. C.; Miller, J. K.; Cle, J.; Whittingham, M. S.; Emsley, L.; Grey, C. P.; Pintacuda, G. Spin-Transfer Pathways in Paramagnetic Lithium Transition-Metal Phosphates from Combined Broadband Isotropic Solid-State MAS NMR Spectroscopy and DFT Calculations. *J. Am. Chem. Soc.* **2012**, *134*, 17178−17185.

(104) Liu, K.; Ryan, D.; Nakanishi, K.; Mcdermott, A. Solid State NMR Studies of Paramagnetic Coordination Complexes: A Comparison of Protons and Deuterons in Detection and Decoupling. *J. Am. Chem. Soc.* **1995**, *117*, 6897–6906.

(105) Helmholz, B. L.; Kruh, R. F. The Crystal Structure of Cesium Chlorocuprate, Cs_2CuCl_4, and the Spectrum of the Chlorocuprate Ion. *J. Am. Chem. Soc.* **1952**, *74*, 1176–1181.

(106) Filip, M. R.; Verdi, C.; Giustino, F. G.W. Band Structures and Carrier Effective Masses of $CH_3NH_3PbI_3$ and Hypothetical Perovskites of the Type $APbI_3$: A=NH_4, PH_4, AsH_4, and SbH_4. *J. Phys. Chem. C* **2015**, *119*, 25209−25219.

TOC GRAPHIC

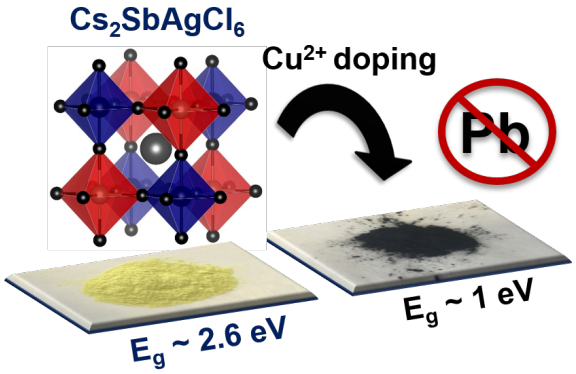

FIGURES

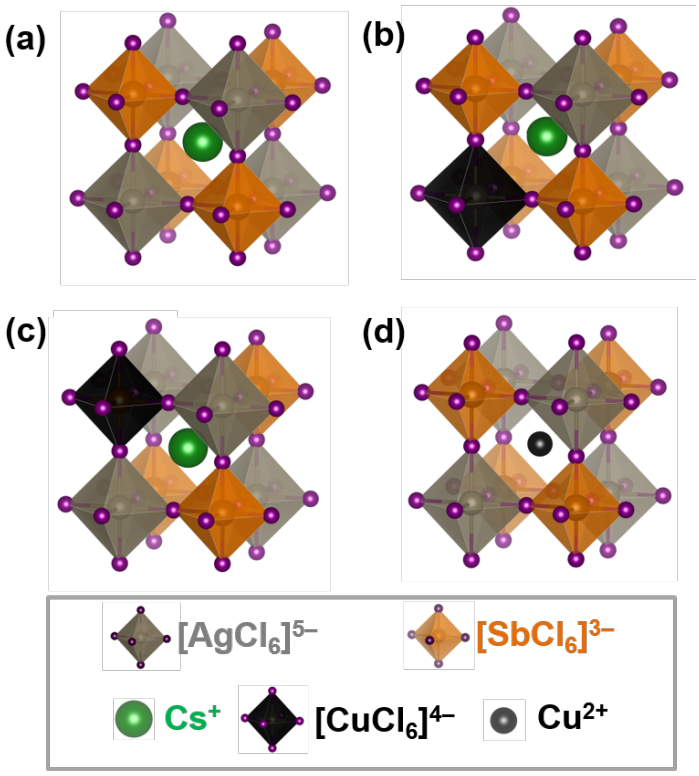

Scheme 1. Schematic representation of the $Cs_2SbAgCl_6$ double perovskite structure (a) and of possible Cu^{2+}-doped analogues where $[CuCl_6]^{4-}$ replaces $[AgCl_6]^{5-}$ (b) or $[SbCl_6]^{3-}$ (c) or where Cu^{2+} replaces Cs^{+} (d); leading to a formation of a neighboring vacancy.

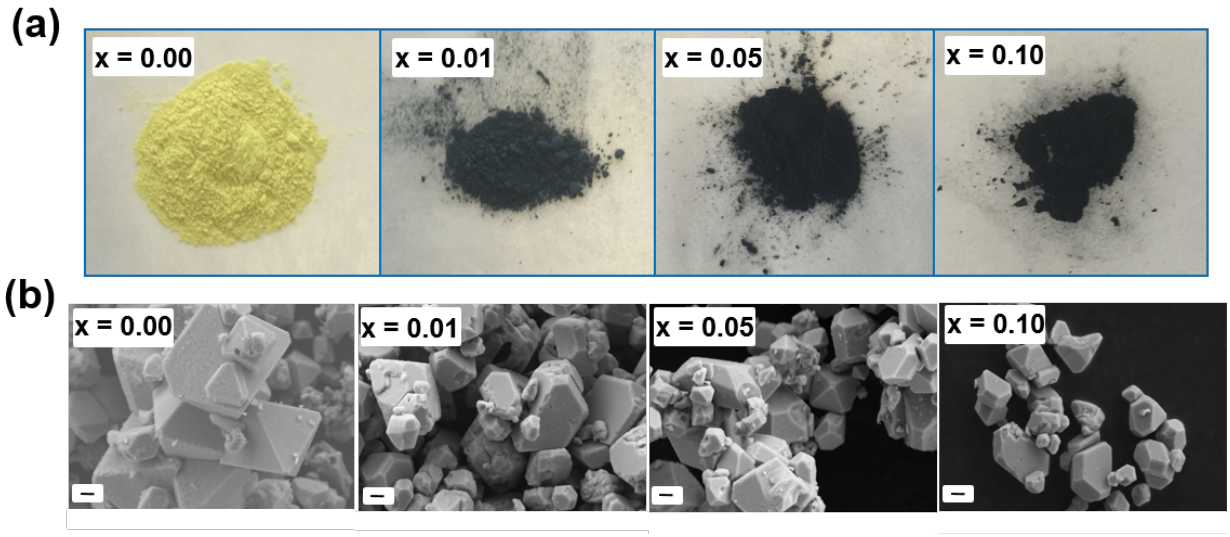

Figure 1. Photographs (a) and FESEM (b) images of $Cs_2SbAgCl_6$ (i.e. x = 0.00) and Cu^{2+}-doped polycrystalline materials. Here, the x values indicate nominal Cu^{2+} loading (see Supporting Information). The scale bar at the lower left of the FESEM images is 2 μm.

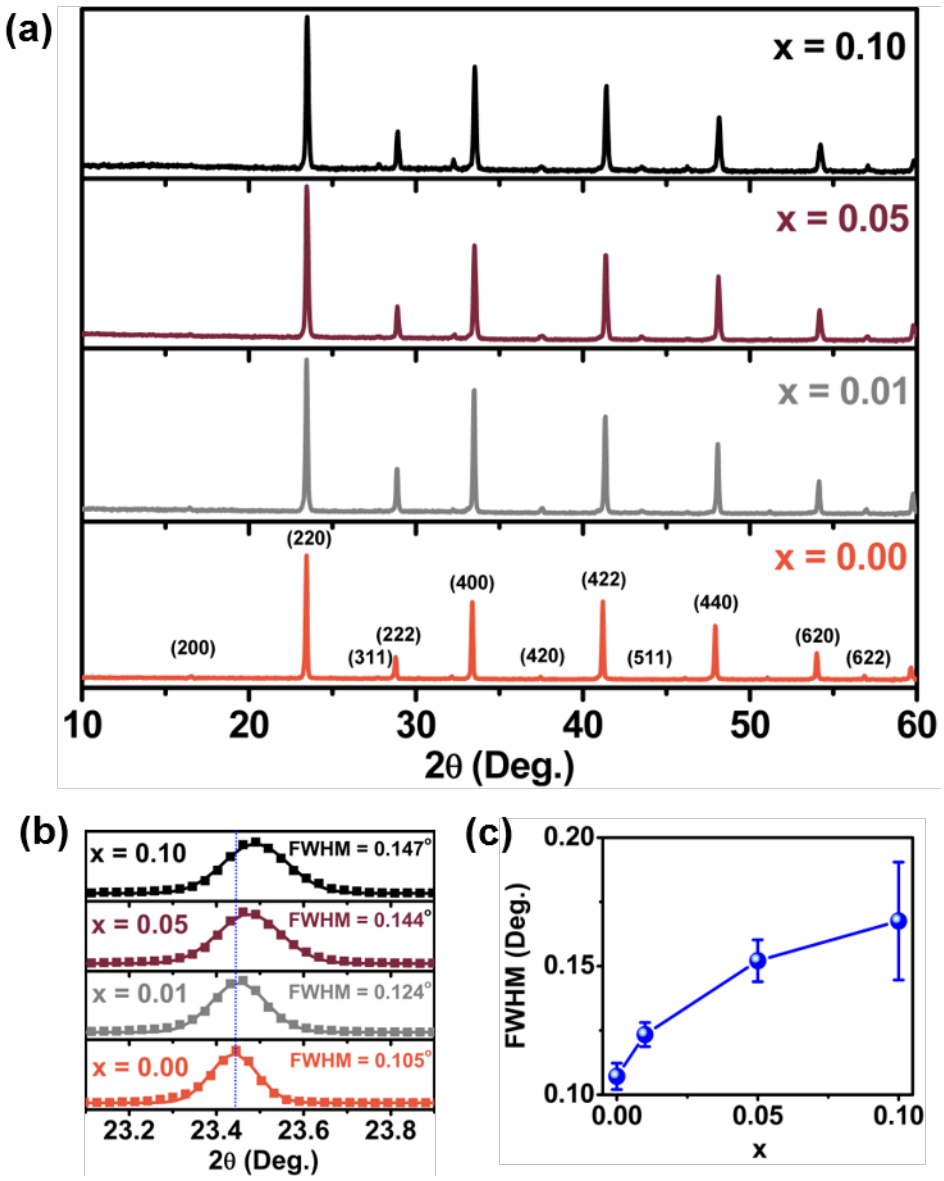

Figure 2. Powder XRD patterns for $Cs_2SbAgCl_6$ (x = 0.00) and for Cu^{2+}-doped $Cs_2SbAgCl_6$ materials (a). An expansion of the highly intense (220) peak in the PXRD patterns are shown in (b), illustrating its shift towards higher 2θ values and its broadening as the Cu^{2+} content increases from x = 0.00 to 0.10. The dotted line is a guide for the eye. FWHM values of PXRD patterns as a function of Cu^{2+} content (x = 0.00 to 0.10) (c).

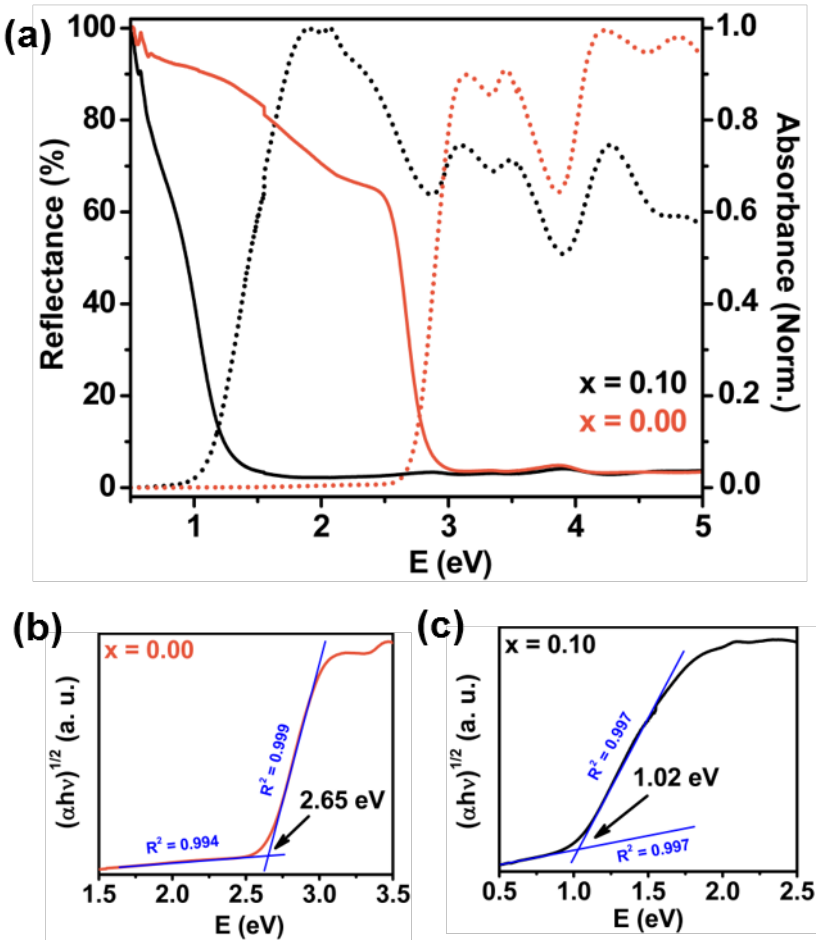

Figure 3. UV-VIS-NIR DR (solid lines) and normalized absorption (dotted lines) spectrum for $Cs_2SbAgCl_6$ parent (i.e. x = 0.00) and the maximum Cu^{2+}-doped (x = 0.10) materials (a). The Tauc plots showing indirect bandgaps of (b) 2.65 eV for $Cs_2SbAgCl_6$ (x = 0.00) and (c) 1.02 eV for the maximum Cu^{2+} doped material (x = 0.10). Please note that DR spectra are converted to absorbance by using the Kubelka-Munk equation (see Supporting Information).

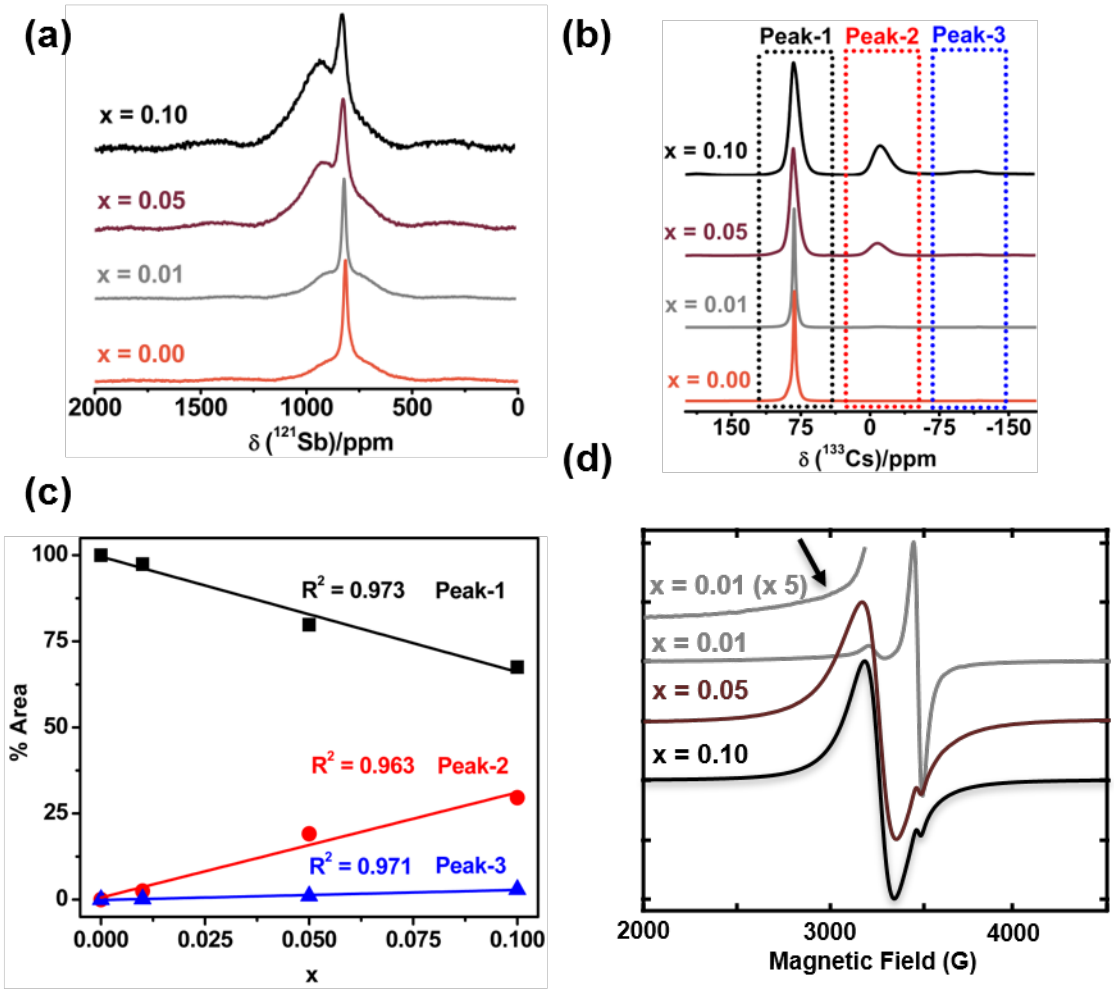

Figure 4. Solid-state ^{121}Sb (a) and ^{133}Cs (b) NMR spectra for $Cs_2SbAgCl_6$ materials with Cu^{2+} doping as indicated; the former spectra were acquired for non-spinning samples at 21.1 T and the latter were acquired at 11.75 T at a spinning frequency of 13.0 kHz. Contributions of three ^{133}Cs MAS NMR peaks to the total area of the ^{133}Cs NMR spectra are shown in (c). X-band EPR spectra of Cu^{2+}-doped $Cs_2SbAgCl_6$ materials (d); the arrow indicates the broad and featureless high field $g_{||}$ component of the signal corresponding to isolated Cu^{2+} sites. Note the data presented in (a) were acquired using a selective 90° pulse to emphasize the higher frequency resonance that is subject to a sizeable quadrupole coupling constant.

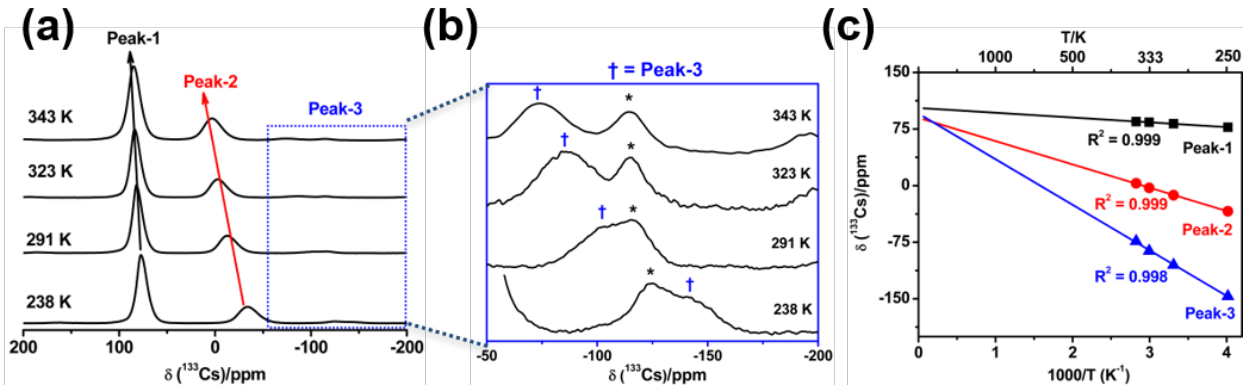

Figure 5. Variable temperature ^{133}Cs MAS NMR spectra of Cu^{2+} doped material (x = 0.10) acquired at 11.75 T with a spinning frequency of 13 kHz (a). Arrows (black and red) are guides to the eye. Temperature dependence of the ^{133}Cs chemical shift of Peak-3 (b); the asterisks (*) and crosses (†) indicate spinning sidebands and Peak-3, respectively. Calculated temperature dependence of the chemical shifts for the three distinct peaks in the ^{133}Cs NMR spectra (c).

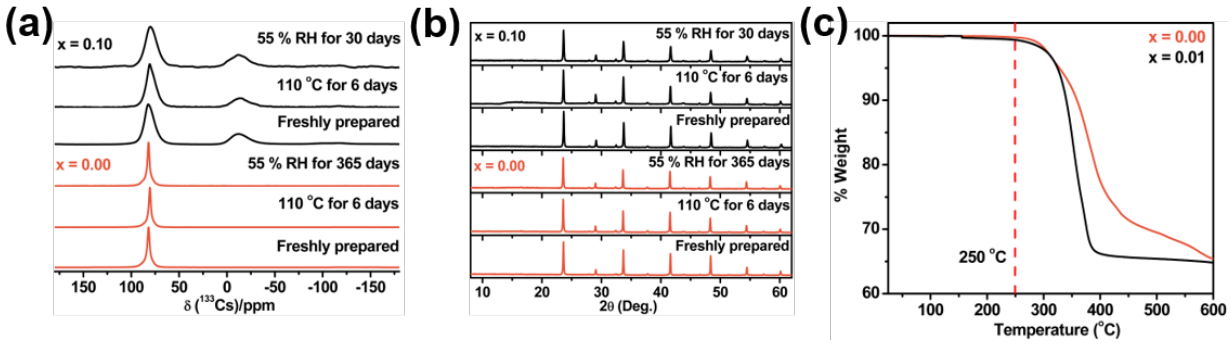

Figure 6. Stability experiments of $Cs_2SbAgCl_6$ parent (i.e., x = 0.00) and the maximum Cu^{2+}-doped (x = 0.10) materials under the indicated conditions: ^{133}Cs MAS NMR spectra acquired at 11.75 T with a frequency of 13 kHz (a), and PXRD patterns (b). TGA analysis data for materials without (x = 0.00) and with trace Cu^{2+} doping (x = 0.01), showing similar thermal stability (c).